Proceedings of ASME Turbo Expo 2023
Turbomachinery Technical Conference and Exposition
GT2023
June 26-30, 2023, Boston, Massachusetts

GT2023-101185

SPATIAL TEMPERATURE AND WATER MOLAR CONCENTRATION MEASUREMENTS USING THERMAL AND ELECTROSTRICTIVE LIGS DURING OPERATION OF A SWIRL BURNER AT PRESSURE

Lee Weller[1,*], Priyav Shah[2], Anthony Giles[3], Francesca De Domenico[4], Steve Morris[3], Benjamin A. O. Williams[2], Simone Hochgreb[1],

[1]Department of Engineering, University of Cambridge, Cambridge CB2 1PZ, UK
[2]Department of Engineering, University of Oxford, Oxford OX1 3PJ, UK
[3]School of Engineering, Cardiff University, Cardiff CF24 3AA, UK
[4]FPT, Aerospace Engineering, TU Delft, Delft, 2629HS, NL

ABSTRACT

Laser-Induced Grating Spectroscopy (LIGS) was applied in a high-pressure combustion facility. Instantaneous (sub-μs), spatially resolved (within 5 mm) measurements of temperature and molar fractions of water were obtained using thermal and electrostrictive LIGS signals. Temperatures up to 1800 K and water molar fractions between 0.01 and 0.12 were measured. A new analytic approach was developed to extract temperature from the frequencies of the measured signal within the flame brush region, where mixtures contain both burnt and unburnt gases. Mean product temperatures are shown to be 8% lower than the adiabatic temperatures for the nominal equivalence ratio, and 14% higher than measurements made with a thermocouple, uncorrected for radiation losses. This work represents the first application of LIGS to a high-pressure, turbulent swirling flame, opening up the potential for future uses in other real world applications. Challenges associated with the deployment of the technique are described, as are potential measures to overcome these difficulties.

Keywords: LIGS, Temperature, Spatial, Thermal, Electrostrictive, Water, High-pressure combustion

NOMENCLATURE

Symbols

γ	Bulk specific heat ratio [-]
Λ	Fringe spacing [μm]
λ_p	Pump wavelength [nm]
ϕ	Equivalence ratio [-]
ρ	Density [kg m^{-3}]
θ	Crossing angle [°]
θ_B	Bragg angle [°]
υ_s	Local speed of sound [ms^{-1}]
f	Modulation frequency [MHz]
g	Ratio of molecular weight to specific heat ratio [kg kmol^{-1}]
n	Mechanism factor [-]
p	Local pressure [Pa]
R	Universal gas constant [J K^{-1} mol^{-1}]
r	Radial location [mm]
T	Temperature [K]
z	Axial location [mm]
W	Molecular weight [kg kmol^{-1}]

Subscripts

a	Air
E	Electrostrictive
P	Products
R	Reactants
T	Thermal

Acronyms

CARS	Coherent Anti-Stokes Raman Spectroscopy
CRZ	Central Recirculation Zone
CW	Continuous-Wave
FFT	Fast Fourier Transform
GTRC	Gas Turbine Research Center
HPOC	High-Pressure Optical Chamber
LIEGS	Laser-Induced Electrostrictive Grating Spectroscopy
LIF	Laser-Induced Fluorescence
LIGS	Laser-Induced Grating Spectroscopy
LITGS	Laser-Induced Thermal Grating Spectroscopy
ORZ	Outer Recirculation Zone
PILOT	Portable In-line LIGS for Optical Thermometry
PIV	Particle Image Velocimetry
SNR	Signal-to-Noise Ratio

*Corresponding author: lw493@cam.ac.uk

Copyright © 2023 by ASME

1. INTRODUCTION

The measurement of scalars such as temperature and concentration of reactants/products in combustion environments using spatially- and temporally-resolved optical diagnostic techniques continues to be of great interest for the validation of models [1–3]. Such measurements demand non-intrusive optical techniques so as not to affect the local conditions. Accurate measurements of scalars are also desired for the design of future internal combustion engines [4–6] and gas turbine combustors [7, 8]. A key challenge is measuring such quantities in turbulent reacting flows at high-pressures and temperatures.

A number of different techniques have been developed to measure scalars, such as temperature and species concentration. Absorption techniques [9] offer fast detection, but poor spatial resolution, spontaneous Raman and Rayleigh scattering [3, 10–12] offer good temporal and spatial resolution, but require high laser energies and specialized noise reduction techniques, while laser-induced fluorescence (LIF) [13] depends on the availability of a fluorescing species. Quantitative measurements demand significant efforts for calibration and corrections owing to interference or signal loss. Non-linear optical techniques, such as Coherent Anti-Stokes Raman Spectroscopy (CARS), offer superior spatial and temporal resolution and higher signal-to-noise ratio (SNR) than the previously described methods, but require specialized high power lasers and complex optical arrangements [14]. A simpler and significantly less expensive non-linear optical technique called Laser-Induced Grating Spectroscopy (LIGS) [15–20] is capable of delivering highly accurate and precise temperature measurements. In addition, the technique has also been used to obtain pressure [21, 22], velocity [23], and molar concentration measurements, both in reacting [24–28] and non-reacting flows [17, 18, 29, 30].

In a typical LIGS experiment, an interference pattern is created within the intersection region of two crossed, coherent pulsed laser beams. The interaction between the laser radiation and molecules within the measurement volume leads to the formation of a transient density grating. This grating can be generated by two different mechanisms. Laser-Induced Thermal Grating Spectroscopy (LITGS) relies on the resonant absorption and subsequent non-radiative release of the laser energy by molecules within the measurement region. On the other hand, Laser-Induced Electrostrictive Grating Spectroscopy (LIEGS) [30] involves the non-resonant creation of the grating via the effect of the electrostrictive force. Both mechanisms generate acoustic waves which propagate across the grating and lead to a modulation of the gas density, and thus the local index of refraction. The dynamics of the transient grating are then probed by a continuous-wave (CW) or long-pulse [18] probe beam that is directed at the grating at the first-order Bragg angle. A small fraction of the probe laser beam is diffracted off the grating with an efficiency that varies in time due to the propagation of the acoustic waves across the grating, generating an oscillating signal beam. The modulation frequency of the transient grating is directly proportional to the local speed of sound, from which the local temperature can be determined. The high precision of the method is derived from the underlying measurement of a temporal frequency which is highly accurate, precise and tolerant of intensity fluctuations. The LIGS signal intensity scales with the local density, so applications in high-pressure environments are attractive.

In this work, we applied the Portable In-line LIGS for Optical Thermometry (PILOT) unit [31] to obtain, for the first time, LIGS measurements in a high-pressure gas turbine research facility (the GTRC in Port Talbot, UK). The compact unit was mounted onto a motorised two axis translation stage for effective mapping of the radial (r) and axial (z) directions. Signals from a premixed methane swirl burner were obtained in the reacting and non-reacting zones for preheated (500 K), medium-power ($\approx$ 68 kW), semi-confined (stainless steel tube with modifications) conditions. Measurements were collected at several radial locations (-55 mm to +55 mm from the central axis) and two axial locations (30 mm and 50 mm from the burner face). These signals were used to determine the statistics of single shot temperature and water molar fractions in the flame region. Suitable temperature averages were also compared to thermocouple measurements.

The paper is organised as follows. The physics of LIGS signal generation and the characteristic features of the collected signals are first discussed. The experimental setup is then introduced, including the combustor system, chemiluminscence setup and the details of the PILOT unit. Next, data analysis procedures to derive temperature (or density) and water molar fractions are presented. Finally, temperature profiles at the two axial locations are compared with thermocouple measurements before providing concluding remarks.

2. THEORETICAL DISCUSSIONS

2.1 LIGS Background

Laser-Induced Grating Spectroscopy is a four wave mixing technique arising from the interference of two pulsed pump beams, a CW or pulsed probe, and a final signal beam. The fringe spacing, Λ, in the interference pattern generated by the two identical beams is calculated from their crossing angle, θ, and wavelength, λ_p,

$$\Lambda = \frac{\lambda_\mathrm{p}}{2\sin(\theta/2)} \,. \tag{1}$$

A coherent probe beam incident at the Bragg angle, θ_B, is used to generate a LIGS signal from within the grating volume. Acoustic waves within the grating volume travel at the local speed of sound, υ_s, and the modulation frequency of the Bragg-scattered LIGS signal is:

$$f = \mathrm{n}\frac{\upsilon_\mathrm{s}}{\Lambda} = 2\mathrm{n}\frac{\upsilon_\mathrm{s}}{\lambda}\sin\left(\frac{\theta}{2}\right), \tag{2}$$

where the factor n is 1 or 2, respectively, depending on whether the mechanism is thermalisation (non-adiabatic) or electrostriction (adiabatic). For perfect gases, the speed of sound can be related to the local properties (temperature, density) and mixture bulk properties as

$$\upsilon_\mathrm{s}^2 = \frac{1}{\mathrm{n}^2}f^2\Lambda^2 = \frac{\gamma RT}{\mathrm{W}} = \frac{\gamma p}{\rho}\,, \tag{3}$$

where γ, W and R are the bulk specific heat ratio, molecular weight of the mixture and universal gas constant, and p, T and ρ are the local pressure, temperature and density, respectively.

Copyright © 2023 by ASME

TABLE 1: Molecular weight and specific heat ratio for air, reactants and products. The adiabatic flame temperature (AFT) and water molar fraction are 1818 K and 0.118 for ϕ = 0.6, respectively. These properties were calculated using Cantera 2.6.0 [32] and GRI Mech 3.0 [33].

	W [kg/kmol]	γ [-]	W/γ [kg/kmol]
air	28.85	1.400	20.61
reactants	28.09	1.368	20.54
products	28.09	1.272	22.09

A straightforward calibration can be used to determine the fixed fringe spacing length, Λ, under non-reacting conditions by measuring the temperature of ambient air, T_a, and the corresponding electrostrictive frequency, f_E.

$$\Lambda = n_E \frac{\upsilon_a}{f_E} = \frac{n_E}{f_E}\sqrt{\frac{\gamma_a R T_a}{W_a}} = \frac{n_E}{f_E}\sqrt{\frac{\gamma_a p}{\rho_a}}\,, \tag{4}$$

where $n_E = 2$, υ_a, γ_a, ρ_a and W_a are the speed of sound, ratio of specific heats, density, and molecular weight of air, respectively.

The density or temperature at any location for which a signal frequency f is measured can be obtained from the calibrated measurements as:

$$T = T_a \left(\frac{n_E f}{n f_E}\right)^2 \frac{\gamma_a}{\gamma}\frac{W}{W_a}\,, \tag{5}$$

$$\rho = \rho_a \left(\frac{n_E f}{n f_E}\right)^2 \frac{\gamma_a}{\gamma}\,, \tag{6}$$

The precision of the frequency measurements, as described in section 4.3, is relatively high (0.7% for ambient air). However, the accuracy of density and temperature measurements depends on (i) the accuracy of the ambient temperature measurements used as a reference and (ii) the accuracy of the estimates of the ratio W/γ. Fortunately, these properties do not vary significantly between air, reactants and products in the present case (see Table 1). The molecular weight varies only by 3%, γ by 9% and W/γ by only 6% between reactant and product. In addition, it is possible to use an iterative interpolation of the values with temperature, leading to higher accuracy of the estimates.

3. EXPERIMENTAL METHODS

3.1 High-Pressure Combustion Rig and Operating Conditions

The fully premixed methane-air swirl burner is housed in a high-pressure optical chamber (HPOC) with rig pressurisation achieved by a back pressure valve. Pressurised gas cylinders provide a fixed methane flow rate of 1.36 ± 0.02 g s^{-1} through Micro Motion ELITE Coriolis mass flow meters. The air flow rate of 39.2 ± 0.2 g s^{-1} was provided and metered with a pair of Bronkhorst M14 Coriolis mass flow controllers. Air was provided by a variable drive speed compressor with an air dryer and two electric preheaters in series. The air was preheated to 500 ± 2 K for the present experiments. Combustion studies were conducted under lean (ϕ = 0.6) conditions and the fuel flow rate was set to maintain a constant power scaling (25 kW/1.1bar) for the pressurised combustion at 3.0 ± 0.1 bar absolute. The burner was first ignited at a stable atmospheric pressure operating condition. The air and methane mass flow rates were then adjusted to increase the pressure to 3 bar while closing the back pressure valve. The geometric swirl number of the burner used for this work was 0.8.

The HPOC allows optical access to the flame through two outer one-inch thick rectangular Spectrosil windows (either side) and a semi-confined 316L stainless steel tube with 100 mm inner diameter and 400 mm length that was machined with a pair of 10 mm × 100 mm (height × length) slots. A detailed description of the experimental rig and design can be found in other work by the authors [34–36].

Temperature and pressure instrumentation within the high-pressure combustion rig are described as follows. A K-type thermocouple was installed on the outside diameter of the metal flame tube at an axial distance ≈ 150 mm from the burner face. The temperature measured during the test was 859 ± 26 K. Room temperatures were also measured as 285 ± 2 K before the test also using a K-type thermocouple. A LIGS comparative temperature at 50 mm downstream from the burner face and at the centerline was measured to be 1437 ± 13 °K using a N-type thermocouple (this value does not take into account radiative heat losses). A Druck PDCR 10/T static pressure transducer was used to measure the pressure within the HPOC. A dedicated data acquisition system was used to log the flow rates, temperature and pressure operating conditions during the experiments.

3.2 OH* Chemiluminescence

The chemiluminescence of excited hydroxyl (OH*) radicals at a wavelength of 310 nm was used as a marker of flame front location and localised heat release. A detailed description of the chemiluminescence camera and data collection has been shown previously [37]. A high-speed camera (Phantom v1212 CMOS camera) coupled to a high-speed image intensifier (SIL40HG50) outfitted with a UV lens (78 mm focal length, F-stop = f/11) and narrow band pass filter (315 ± 15 nm) was used to capture the OH* signals.

The image plane was centred on the burner exit nozzle, with respective view fields of 100 mm in both the radial and axial direction, with an image resolution of approximately 5 pixels mm^{-1}. Note that the chemiluminesence and LIGS experiments were not carried out at the same time. For the chemiluminescence experiments, the swirl burner was fully confined by a quartz tube instead of the modified stainless steel tube. Average images were obtained from 2000 background corrected images (image intensifier gated at 10 μs) for the fully premixed methane case at a rate of 4 kHz (sample time = 0.5 s). A modified open-access Abel inversion algorithm [37] was used to transform the averaged images into planar representations of the OH* chemiluminescence intensity distribution, assuming cylindrical symmetry.

3.3 PILOT System

The PILOT unit was used to perform LIGS measurements in the HPOC. The system is capable of obtaining tracer-free LIGS measurements at repetition rates of up to 400 Hz. It produces

Copyright © 2023 by ASME

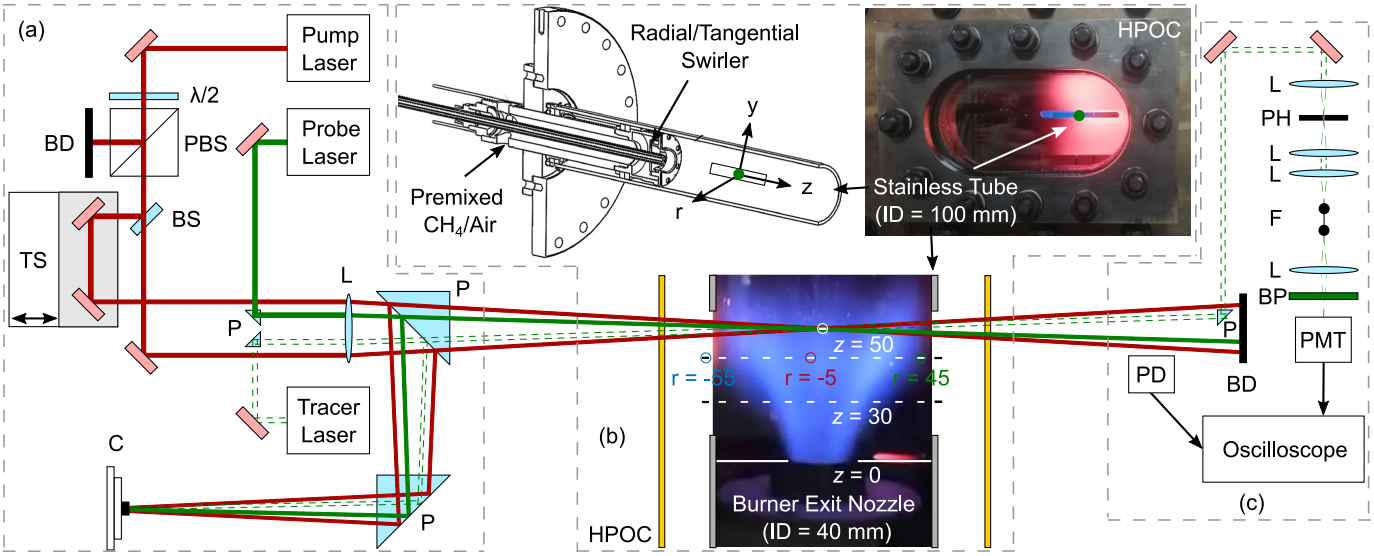

FIGURE 1: Schematic of (a) the PILOT unit, showing the path of the pump, probe and signal tracing beams, along with (b) a schematic of the high-pressure optical casing (HPOC) and (c) back-end collection optics. Pump Laser: 1064 nm pulsed laser; Probe Laser: 532 nm CW laser; Tracer Laser: 532 nm DPSS Laser; PBS: Polarisation Beam Splitter (for 1064 nm); $\lambda/2$: Half-Wave Plate; TS: Translation Stage; BD: Beam Dump; BS: Beam Splitter (for 1064 nm); C: Camera; P: Prism; L: Lens; PD: Photodiode; F: Fiber; PMT: Photomultiplier Tube; BP: Band-Pass Filter (for 532 nm); PH: Pin Hole;

pump beams at 1064 nm (Nd:YAG Quantel Merion C laser) with an adjustable energy of up to 35 mJ per beam delivered over 10 ns. The wavelength and energy allow for tracer-free electrostrictive and water-thermal LIGS measurements. A Verdi V-18 laser from Coherent was used as the probe laser, producing a probe beam at 532 nm with an adjustable power of up to 18 W. Figure 1 shows a schematic of the PILOT unit along with the HPOC and back-end collection optics. The design and characterisation of the unit has been previously discussed [31].

The PILOT unit was mounted on a 2-axis motorised translation stage. The detection rail, containing the signal detection optics for the PILOT unit, was attached to the same frame on the opposite side of the HPOC so that it could be translated in tandem with the beam delivery unit. The translation stage was fixed onto a single Unistrut platform attached to the bedrails underneath the HPOC. This design ensured that the PILOT delivery and detection optics would not be affected by vibrations of the rig during operation. The PILOT unit, as well as the motorised translation stages, were run remotely from another room to ensure safety during operation.

A spatial filter was introduced onto the detection rail to reject reflected light from the HPOC windows and thus improve the SNR ratio of the LIGS signals. The spatial filter consisted of two lenses, each with focal length f = 100 mm, separated by 200 mm with a pin hole (250 μm) placed at the mid-point between them. The LIGS signals were collected by a Hamamatsu H10721-20 photomultiplier tube and digitised by a Picoscope 6402 oscilloscope (8-bit channel at 500 MHz) from Pico Technology. A photodiode (Thorlabs DET210) was used to detect the pump beam and trigger the acquisition of the LIGS signals by the oscilloscope. The signals were acquired at 10 Hz for a total of 100 seconds at each test point.

4. LIGS TIME AND FREQUENCY CHARACTERISTICS

4.1 Signal Processing Steps

Signals obtained by the oscilloscope were processed to determine the frequencies and ratios present according to the following procedure:

1. A raw signal, S_i, as a function of time t typically consists of an array of 1260 data points collected at 2.5 GS/s. An ensemble of single shots in the reactant and product regions is shown in Fig. 2.

2. Each single shot voltage-time array was organised for extraction of the signal frequency, f as follows. First, the signal was zero-padded to a length of 2^{19} points. A windowing function (Hann or raised cosine) was then used to smooth out the padding at the edges and a nonlinear filter (Wiener-2) was applied to remove high frequency noise. The FFT was applied to the modified signal to obtain the individual power spectrum, $\hat{S}_i(f)$.

3. Peak frequencies in the power spectrum, $\hat{S}_i(f)$ between 20 to 90 MHz are expected as thermal and electrostrictive signal frequencies for the given beam crossing geometry [31]. The magnitude of these peaks were interpreted as the characteristic intensity of the signal in the analysis of dominant frequencies.

4. Once the frequencies were determined, it was possible to classify them either as thermal (< 45 MHz) or electrostrictive (> 45 MHz). This determines the n value to be used in Eq. 5 when finding temperature.

5. The molar concentration of water was determined from the calibrated ratio of the second peak intensity (thermal) to that

Copyright © 2023 by ASME

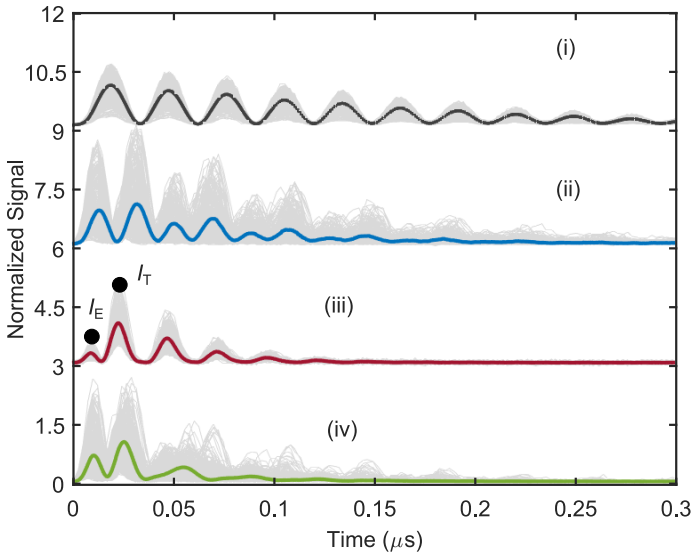

FIGURE 2: Measured normalized single-shots (gray) and average (color) LIGS signals for radial locations (i) 0 mm (ambient air only), (ii) -55 mm, (iii) -5 mm and (iv) 45 mm at a axial location of 50 mm away from the burner face. Each plot is shifted vertically by three units for clarity. The labels I_E and I_T represent the electrostrictive and thermal peak magnitudes, respectively.

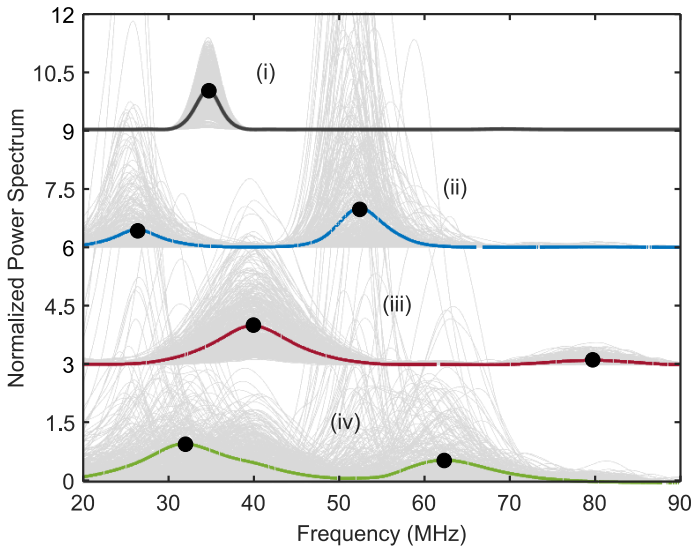

FIGURE 3: Measured normalized single-shots and normalized averaged FFT signals for the LIGS signals in Fig. 2. Each plot is shifted vertically by three units for clarity.

of the first peak (electrostrictive) within the LIGS voltage-time signal (see Fig. 2 for illustration) as described in the method by [26], using the equilibrium value of the molar fraction of water vapor as a reference. The magnitude of the first and second peak were extracted from the modified LIGS signal by using a peak finder function between two different times.

4.2 Time Domain Signal Characteristics

The LIGS signals were extracted and processed in the manner described above. Signals from different flame regions exhibit different frequencies, as well as different signatures (or shapes) associated with their composition and thus balance of thermal and electrostrictive content. Four different characteristic signals were identified.

Figure 2 shows the measured normalized single-shots and normalized averaged LIGS signals as a function of time. Each plot consists of N = 1000 raw LIGS signals (gray solid lines). The single-shots, $S_i(t)$, and average signals, $\sum_{i=1}^{N} S_i(t)$ / N, are normalized by the magnitude of the average peak height, $\sum_{i=1}^{N} \max(S_i(t))$ / N. Each plot was shifted vertically by three units for clarity. The black solid line in Fig. 2 (i) shows the signature in air at ambient temperature, which was used for calibration. The ambient air signal is purely electrostrictive, showing many oscillations over the time duration of 300 ns. The measurement was taken at the center of the HPOC just above the location of the N-type thermocouple, in the absence of any flame. It is clear that there was little variation in the signal characteristic (and in particular, frequency) at a constant temperature. The magnitude variation was the result of shot-to-shot fluctuations in pulse energy, window residue and dust within the measurement volume.

The blue solid line in Fig. 2 (ii), obtained in the region near the outer recirculation zone of the flame (z = 50 mm, r = -55 mm), shows a combined electrostrictive and thermal signature. The thermal component, identified by the increased magnitude of every other peak (as it oscillates at half the frequency of the electrostrictive component), is produced by the absorption of water vapor that has recirculated back into the measurement volume from the product zone. The mixed gas is hotter than the incoming heated gas, so that the electrostrictive frequency is higher than that obtained in case (i) at ambient temperature. The magnitude of the (non-normalized) signal is lower and decays more quickly than is the case at the lower temperatures.

The red solid line in Fig. 2 (iii) was obtained in the flame product region (z = 50 mm, r = -5 mm), and represents a predominantly thermal signature with water, inherently produced during combustion, as the absorbing species. Although all signals shown are normalized, the SNR of the signal improves significantly in the presence of water vapor. This is also highlighted by the decrease in variance from shot to shot. Therefore, even for a reduced time duration of 150 ns, several oscillations can be resolved. The first peak corresponds to the electrostrictive signal with magnitude I_E, and the following peaks are dominated by the thermal signal, starting with the second peak of magnitude I_T. The ratio $R = I_T/I_E$ is used in section 5.2 as an indicator for the presence of water vapor.

The green solid line in Fig. 2 (iv) represents a signal with both thermal and electrostrictive features, acquired in the region of the turbulent flame brush (z = 50 mm, r = 45 mm) in which both products and reactants are present. In this case, it is more difficult to interpret the signal: oscillations are present, but the thermal signal is smaller than in the case of the product zone resulting in fewer and less well defined peaks.

4.3 Frequency Domain Signal Characteristics

Figure 3 shows the normalized single-shot and normalized averaged power spectra as a function of frequency for the four

Copyright © 2023 by ASME

cases described in Fig. 2. Each plot consists of N = 1000 raw power spectra (gray solid lines). The single-shots, $\hat{S}_i(f)$, and averaged transformed signals, $\sum_{i=1}^{N} \hat{S}_i(f)/N$, are normalized by the average magnitude of the power spectrum, $\sum_{i=1}^{N} \max(\hat{S}_i(f))/N$. Each plot is shifted vertically by three units for clarity.

The power spectrum for ambient air in Fig. 3 (i) shows a peak frequency value of 35.1 ± 0.2 MHz for a purely electrostrictive signal, which corresponds to a fringe spacing of Λ = 19.2 ± 0.1 μm (using Eq. 4), at the calibration temperature T_0 = 285 ± 2 K. The width of the frequency peak is determined by the spread in peak frequencies for the corresponding LIGS spectra over the 1000 shots (see Fig. 4). The LIGS signals at ambient conditions show many oscillations and a stable temperature, and thus result in a relatively narrow peak frequency.

Figure 3 (ii) shows two frequency peaks. The electrostrictive peak frequency has increased to 52 ± 1 MHz, corresponding to the higher temperature in the outer recirculation zone (ORZ). A second peak of about half the magnitude of the electrostrictive one appears at 26 ± 1 MHz. This thermal signal arises from the absorption of water in the recirculation zone. Both peaks are wider than that recorded in ambient air, reflecting a broader range of temperatures. Figure 3 (iii) shows a thermal peak frequency at 40 ± 1 MHz, clearly at higher frequencies than (ii) corresponding to the higher temperatures in the product zone region. A very small electrostrictive contribution (higher frequency peak in Fig. 2 (iii)) sits around 80 ± 1 MHz is also observed.

Finally, Fig. 3 (iv) shows the power spectrum for the region in the flame brush. A thermal LIGS peak is identified at 32 ± 2 MHz, and a weaker electrostrictive signal at 62 ± 2 MHz. The signature is a superposition of both thermal and electrostrictive frequencies from (ii) and (iii), and there is clearly a much larger spread of obtained frequencies, corresponding to a mixture of temperatures and gas compositions.

5. PROBABILITY DISTRIBUTIONS OF FREQUENCIES AND RATIOS

The turbulent combustion system considered is expected to show fluctuations in temperature and water concentrations, depending on the location of the measurement volume. The fluctuations are reflected in the frequencies and magnitudes of electrostrictive and thermal LIGS signals. In this section, we propose a binning technique to analyse the probability distributions of the frequencies (corresponding to temperatures) and the ratio of the magnitudes of the thermal to electrostrictive signal (corresponding to the molar fraction of water vapor). The procedure is described as follows.

The individual power spectrum for each of the shots, $\hat{S}_i(f)$, often contains peaks for more than one frequency above a minimum threshold, $\hat{S}_i(f_j) > P_0$. Care must be taken to ensure that higher order frequencies, which may occur due to signal noise, are not mistaken for real peaks within the analysis. Occasionally, it is necessary to manually inspect the results to ensure that no false values are extracted.

The value of each peak frequency, f_j, the ratio of the peak thermal to electrostrictive signal magnitude, R_j, and its corresponding power spectrum intensity, P_j, are then used to weigh the histogram into 200 bins (between 20 to 90 MHz, with bin size 0.35 MHz for the frequencies, and from 0.75 to 7.5 with bin size 0.03 for the ratios). The peak mode for the distribution so constructed is used to normalise the histogram at each location. Note that since a single shot may contain several frequencies, the total number of frequencies exceeds the number of shots.

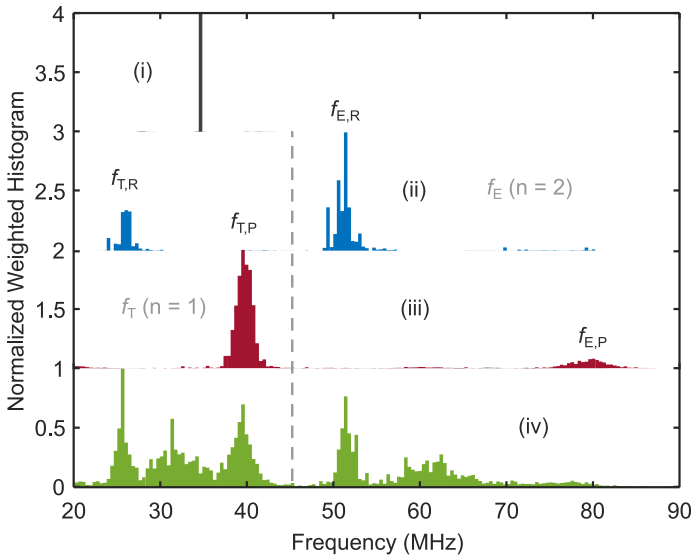

FIGURE 4: Measured normalized weighted frequency histograms for the LIGS signals in Fig. 2. Each plot is shifted vertically by unity for clarity.

5.1 Frequency distribution

Figure 4 shows the normalized weighted frequency histograms for 1000 shots at the four radial cases described in Fig. 2. In Fig. 4 (i) the purely electrostrictive calibration measured frequency value is 35 MHz. For the reacting case (z = 50 mm, r = -55 mm), Fig. 4 (ii) shows predominantly electrostrictive frequencies, with lower thermal frequencies and peak values of 51 MHz and 26 MHz, respectively. The radial location near the centerline (z = 50 mm, r = -5 mm) Fig. 4 (iii) shows primarily thermal and electrostrictive frequencies in the product zone, with peak frequency values of 40 MHz and 80 MHz, respectively.

Figure 4 (iv) (z = 50 mm, r = 45 mm) shows a more complex frequency distribution. Measurements show frequencies associated with both thermal and electrostrictive product zone and reactant zone signals as seen in (ii) and (iii). In addition, further frequencies appear at 31 MHz and 62 MHz. These are clearly harmonics, but their interpretation is not entirely clear, although it may represent a weighted averaged of the frequency associated with a mixture of burned and unburned gases in the measurement volume.

5.2 Peak ratio distribution

Figure 5 shows the distribution of the ratios $R = I_T/I_E$ for 1000 shots at the four radial locations described in Fig. 2. The magnitude in each bin is normalized by the peak magnitude in the histogram. In a previous study in a laminar flame [26], the magnitude of the ratio, R, was shown to be proportional to the molar fraction of water vapor, X_{H_2O}, for thermal signals, so these

Copyright © 2023 by ASME

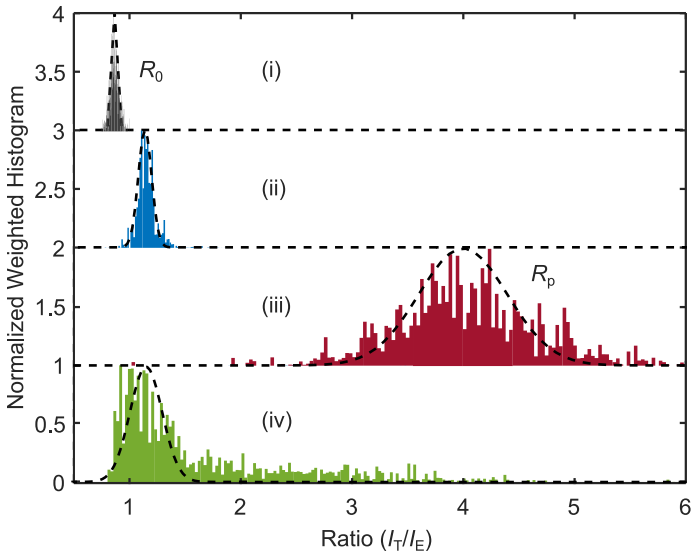

FIGURE 5: Measured normalized weighted histograms of the ratio $R = I_T/I_E$ for the LIGS signals in Fig. 2. Each plot is shifted vertically by unity for clarity.

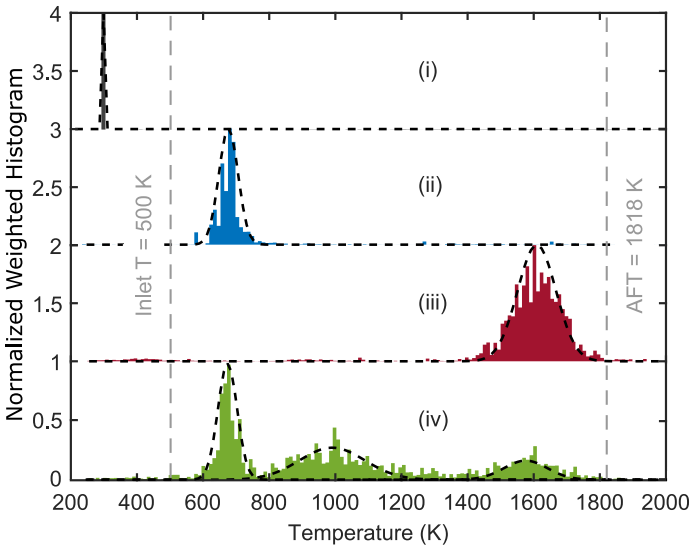

FIGURE 6: Calculated normalized weighted temperature histograms for the LIGS signals in Fig. 2. Each plot is shifted vertically by unity for clarity.

can be calibrated assuming equilibrium conditions in the product zone, to determine the value of the water vapor fraction.

Figure 5 (i) shows the measurements of the ratio R corresponding to ambient air. The thermal signal is too low owing to the the low moisture in ambient air, and the results represent an effective zero value, $R_0 = 0.87 \pm 0.04$. This is later used to correct for the electrostrictive component (assuming the same electrostrictive ratios at different temperatures). In section 6.3 we use corrected measured ratio values $R - R_0$ to work out the molar fraction of water vapor.

For case (ii), the mean ratio value is 1.16 ± 0.08, suggesting a relatively narrow deviation of the molar fractions of water vapor. The narrow distribution is somewhat surprising, as one would expect variable mixedness with the product gases in the outer recirculation zone. In case (iii) corresponding to the product zone, the measured ratio and standard deviation is 4.0 ± 0.7. The larger value of the mean ratio reflects the higher value of the molar fraction of water vapor in the products. The larger standard deviation is more difficult to explain, as the product composition should have little fluctuation in water content. However, it is possible that there is still turbulent mixing with the surrounding unburned mixture, as well as some of the air exiting through the slots created for beam delivery.

Finally, Fig. 5 (iv) shows a measured ratio distribution of 1.2 ± 0.3 for the region at a radial location of 45 mm near the flame brush. The relative contribution of thermal and electrostrictive signal depends on the concentration and temperature of water from the products and unburnt air within the same measurement volume. The mean ratio value in this mixing region is dominated by reactants and the electrostrictive mechanism, even though the distribution also shows higher ratio values were measured. The relatively low incidence of ratios associated with the product appears to indicate that most of the measurements in this location are associated with reactant rather than product.

5.3 Temperature distribution

The measured frequency values from the previous sections can be converted into temperature values using Eq. 5. Table 1 shows that the value of the ratio of molecular weight to specific heat ratio, $g = W/\gamma$ varies from 20.54 kg/kmol for the reactants, g_R, to 22.09 kg/kmol for products, g_P, or a change of 6%. For premixed flames, it is assumed that the change in properties varies linearly with the progress of reaction and thus temperature. Since the temperature varies as the square of frequency, we have:

$$\frac{g - g_R}{g_P - g_R} = \frac{f_T^2 - f_{T,R}^2}{f_{T,P}^2 - f_{T,R}^2}\,, \tag{7}$$

where $f_{T,R}$ and $f_{T,P}$ are the mean measured thermal reactant and product frequency values from Fig. 4. Note that the same interpolation was carried out for the case of the electrostrictive frequencies.

Figure 6 shows the normalized weighted temperature histograms for 1000 shots at the four different radial locations in Fig. 2. The normalization follows the same procedure as in Figs. 4 and 5. The temperatures are calculated from the frequencies in Fig. 4 with a factor n = 1 or n = 2 used for thermal and electrostrictive frequencies below and above 45 MHz, respectively, and the g values equal to the interpolated values from Eq. 7.

Figure 6 (i) shows the temperature distribution corresponding to 285 ± 2 K for room air, after the calibration value was used for the mean temperature. Figure 6 (ii) shows values for the temperature in a region outside the flame brush region (z = 50 mm, r = -55 mm) in a region involving recirculation of products and entrained reactants. The mean value is equivalent to 680 ± 15 K. The signal is predominantly electrostrictive, and the properties of the gases are assumed to be close to that of reactant gases. In the case of the location in the product zone (iii), the calculated mean temperature 1610 ± 30 K, the signal is predominantly thermal, and the value of g close to that of the products. The temperature

Copyright © 2023 by ASME

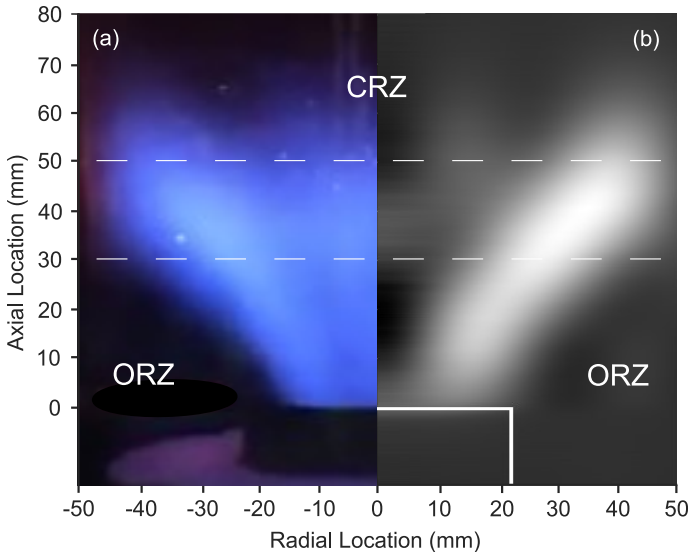

FIGURE 7: Premixed methane swirl burner for (a) visible camera image and (b) Abel-transformed OH* chemiluminescence image as a function of axial and radial locations.

compares with an adiabatic temperature of 1818 K for the particular stoichiometry used. We note that there are heat losses owing to the conduction and radiation of the product gases outside of the metal tube, and that there may be some entrainment of colder gas from the region between the inner cylinder and the outer chamber during the experiment.

Finally, at the radial location of 45 mm (iv) shows three temperature modes in the distribution. The lower and upper modes correspond to the product and reactant temperatures. The third mode centered at 1000 ± 50 K is most likely a combination of product and reactant gases. The relatively large deviation for the particular mode shows there are a significant number of situations with different combinations of both temperatures.

6. SPATIAL TEMPERATURE PROFILES

6.1 Spatial Chemiluminescence Images

Figure 7 shows a color camera image (a) and OH* Abel-deconvoluted chemiluminescence image (b) for two halves of the premixed methane swirl burner. Typical flow fields for this premixed swirler configuration have been shown previously using Particle Image Velocimetry (PIV) [38]. The outward flow from the burner exit nozzle (ID = 40 mm) generates a conical flame structure around a central recirculation zone (CRZ) and shear layer of zero axial velocity. Outside the outer shear layer, an outer toroidal recirculation zone (ORZ) is produced near to the walls, with regions of both products, entrained reactants, and mixtures of both.

Figure 7 (a) and (b) shows at an axial location of z = 30 mm the flame brush regions have not yet reached the wall, and that beyond radial locations of ± 35 mm one can expect to observe regions of ORZs involving products and reactants. For radial locations within the CRZ for r ± 15 mm mostly products (and therefore water) can be expected. For an axial location of approximately 40 mm the flame brushes reach the wall and ORZs can no longer be expected within the confined geometry. For

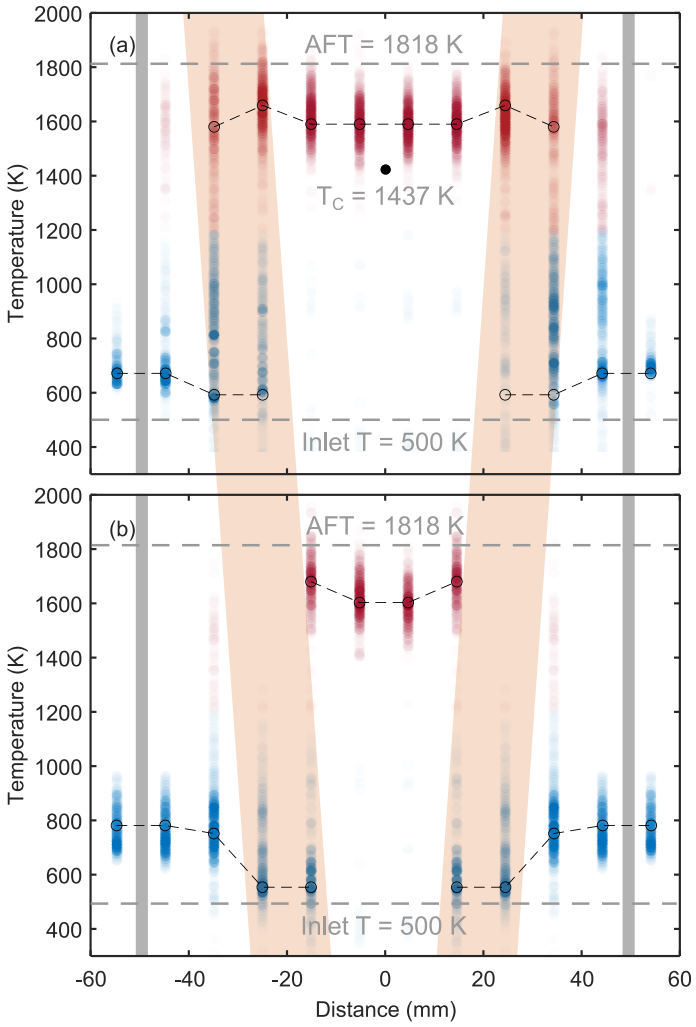

FIGURE 8: Extracted temperature measurements as a function of radial distance at two downstream axial locations of (a) 50 mm and (b) 30 mm from the burner face. The colors indicate predominantly thermal (red) or electrostrictive (blue) LIGS signatures, respectively, and the intensity indicates the magnitude of the normalized bar charts in Fig. 6. The gray lines highlight the location of the stainless steel walls.

an axial location of z = 50 mm the CRZs and purely product regions dominated by water are expected within radial locations ± 30 mm.

6.2 Spatial Temperature Profiles

Figure 8 shows the calculated temperature obtained from the frequency measurements, as a function of radial location at the two axial locations of (a) 50 mm and (b) 30 mm from the burner edge. The colors indicate predominantly thermal (red) or electrostrictive (blue) LIGS signatures, respectively. The intensity of the symbol color is proportional to the normalized bar charts shown in Fig. 6.

Figure 8 (a) shows the temperature profile in the furthermost downstream region at 50 mm from the burner face. The lowest temperatures are around 600 K, a value which is higher than the inlet heater temperature of 500 K. This means that the reactants

Copyright © 2023 by ASME

partially mix with products before they move into the flame region. This is clear from the temperatures in the ORZ near the walls, which are also higher than those of the incoming air, reaching 650 K. As shown in section 6.3, the presence of water vapor in this region is consistent with the temperature result. Measurements are registered in a region which geometrically should be nominally outside the reacting zone. This would suggest that it would be possible for the hotter ORZ gases to leak out the slot windows in the tube, causing this result. The PILOT unit is estimated to have a spatial resolution of 6 mm × 0.3 mm × 0.3 mm [31]. Therefore, there is an uncertainty in the position of the measurement volume in the radial direction of the order of 6 mm, so the locations may reflect temperatures inside rather than outside the tube.

The peak measured temperatures appear near the edge of the recirculation zone of the swirling flame, with a measured value of 1680 ± 70 K at a radial distance of -25 mm and 25 mm. This compares to a calculated adiabatic flame temperature of 1818 K for the particular equivalence ratio of 0.6, reactant inlet temperature of 500 K and pressure of 3 bar. The temperatures at the centerline are slightly lower, of the order of 1610 K. Such a temperature profile with a dip at the centerline is consistent with cooler gas entrainment into the CRZ, leaving a peak near the flame brush. Thermocouple temperatures (uncorrected for radiation heat losses) of 1437 ± 13 K are approximately 200 K lower than the measured LIGS temperatures within the CRZ.

Figure 8 (b) shows the temperature profile for a region 30 mm downstream from the burner face. The minimum temperature of 550 K appears near the outer radius of the inlet of the swirl burner, and is close to the nominal inlet gas temperature of 500 K. Further outwards, the temperatures reach almost 800 K. This again appears to reflect the entrainment of the reactants with the burned gas in the ORZ. We note that the temperatures in the outer zone at this position are higher (780 K) than those further downstream. This suggests that there is a higher fraction of products of combustion in this region than the position further downstream at the same radius. This is also consistent with the fraction of water vapor shown in section 6.3. The peak temperatures appear again near the edge of the flame brush, with a small dip near the centerline, common for a flame with a CRZ. Measured mean values are once again slightly lower than adiabatic temperatures.

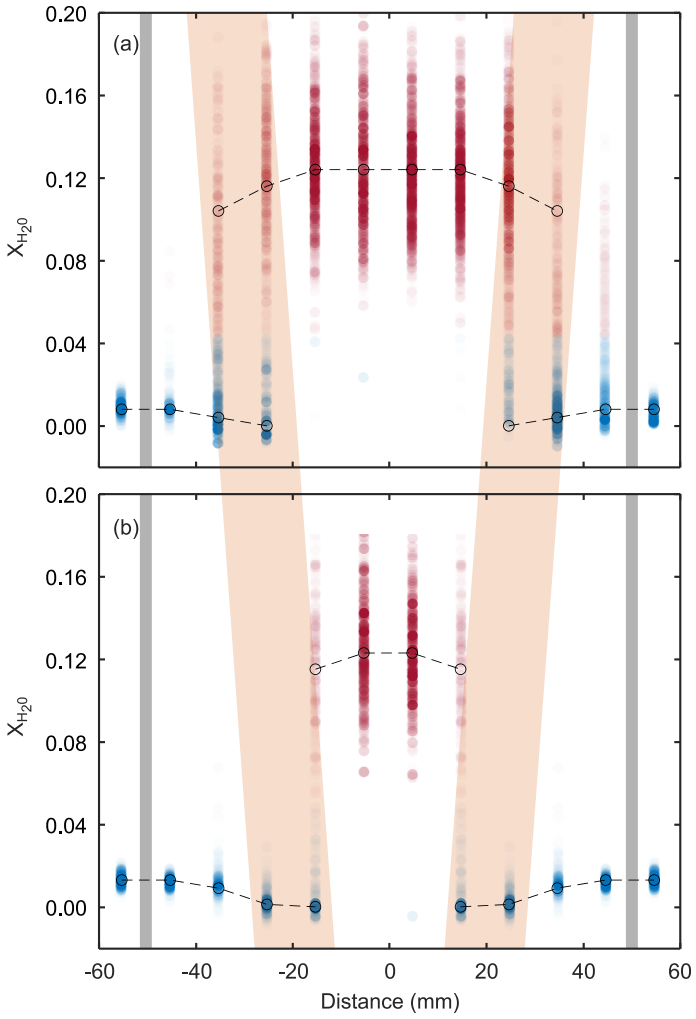

FIGURE 9: Molar fraction of water vapor as a function of radial locations at axial distances of (a) 50 mm and (b) 30 mm from the burner edge. The colors indicate predominately thermal (red) or electrostrictive (blue) LIGS signatures, respectively, and the intensity indicates the magnitude of the normalized bar charts. The gray lines highlight the location of the stainless steel walls.

6.3 Spatial Profile of Molar Fraction of Water Vapor

The corrected measured ratios of thermal to electrostrictive intensities R, and the zero ratio R_0 corresponding to ambient air (see Fig.5) were used to determine the approximate water molar fraction. The mean values of the maximum ratio difference in the product region, $R_P - R_0 = 3.1 \pm 0.7$ were associated with values obtained from the equilibrium water molar fraction for the current stoichiometry, $X_{H_2O} = 0.12$ (see Table 1). All other values of $R - R_0$ were scaled linearly to deliver the corresponding molar fraction of water vapor for each shot. A systematic uncertainty of course arises from this assumption.

Figure 9 shows the measured and scaled molar fraction of water vapor as a function of radial location at axial positions of (a) 50 mm and (b) 30 mm from the burner face. The colors indicate predominantly thermal (red) or electrostrictive (blue) LIGS signatures, respectively. The intensity of the color is related to the corresponding normalized intensity of the histograms shown in Fig. 5.

Figure 9 (a) shows maximum water molar fractions of 0.12 for the product zones, and minimum fractions for the zones where reactants unmixed with product should be found. Note that the molar fractions of water vapor do not decrease in the centerline of the CRZ, unlike the temperature. The entrained gases in the CRZ may have been in contact with the outer walls, leading to proportionally more heat losscompared to water vapor, which is conserved. A similar pattern is seen in Fig. 9 (b), but with a smaller product zone, and a slightly lower molar fraction appearing in the region where the fresh reactants enter the zone (without entrained water vapor), as would be expected.

Copyright © 2023 by ASME

7. CONCLUSIONS

LIGS has been implemented in a high-pressure gas turbine research facility for the first time, providing spatially resolved temperature and water vapor concentration measurements for academic and industrial use. A portable LIGS unit, outfitted with pump beams at 1064 nm, has been deployed for tracer-free measurements at elevated pressure, using electrostrictive and thermal signals from water vapor. In addition, a revised weighted normalized binning data processing method has been implemented to process the LIGS signals obtained in the turbulent flames.

At the radial centre of the swirl burner, the reactants are fully burned and the spectrum is dominated by a thermal water vapor signature with a molar fraction of approximately X_{H_2O} = 0.12 and a temperature on the order of 1600 K. Moving further out from the centre towards the flame brush, the temperature increases until it reaches a maximum within the centre. Here temperature values on the order of 1650 K were measured, with a slight decrease in the amount of water vapor. At this location, the spectrum takes the form of three signatures: a hot thermal signature similar to the fully burnt zone, a hot electrostrictive signature with recirculated water vapor, and a third signature, which contains a combination of both, dictated by the mechanism involved and the mixing of burnt and unburnt gases within the measurement volume. A more refined approach was developed to interpolate mixture properties between those of reactants and products, allowing the presentation of the combined temperature results within the flame brush.

The successful implementation of LIGS in a turbulent reacting flow opens up the possibility of using the technique in model and sector gas turbine combustors, allowing temperature measurements to improve the understanding and control of NO_X emissions.

ACKNOWLEDGMENTS

Lee Weller, Priyav Shah and Anthony Giles are funded under EPSRC UK Award EP/T030801/1 within the LIGS project. Francesca De Domenico acknowledges the support of Gonville and Caius College via the Junior Research Fellowship.

We are grateful to Daniel Eakins and David Chapman at Oxford for loan of the Verdi V-18 laser from Coherent. The datasets associated with this article are available at the following DOIS (10.17863/CAM.94523 and 10.17035/d.2023.0237814302) or from the corresponding author on request.

For the purpose of open access, the authors have applied a Creative Commons Attribution (CC BY) licence to any Author Accepted Manuscript version arising from this submission.

REFERENCES

[1] Aldén, Marcus, Bood, Joakim, Li, Zhongshan and Richter, Mattias. "Visualization and understanding of combustion processes using spatially and temporally resolved laser diagnostic techniques." *Proceedings of the Combustion Institute* Vol. 33 No. 1 (2011): pp. 69–97.

[2] Jeffries, Jay Barker and Kohse-Hoinghaus, Katharina. *Applied combustion diagnostics*. Taylor & Francis (2002).

[3] Eckbreth, Alan C. *Laser diagnostics for combustion temperature and species*. Vol. 3. CRC press (1996).

[4] Williams, Ben, Edwards, Megan, Stone, Richard, Williams, John and Ewart, Paul. "High precision in-cylinder gas thermometry using laser induced gratings: quantitative measurement of evaporative cooling with gasoline/alcohol blends in a GDI optical engine." *Combustion and flame* Vol. 161 No. 1 (2014): pp. 270–279.

[5] Scott, Blane, Willman, Christopher, Williams, Ben, Ewart, Paul, Stone, Richard and Richardson, David. "In-cylinder temperature measurements using laser induced grating spectroscopy and two-colour PLIF." *SAE International Journal of Engines* Vol. 10 No. 4 (2017): pp. 2191–2201.

[6] Förster, Felix, Crua, C, Davy, Martin and Ewart, Paul. "Temperature measurements under diesel engine conditions using laser induced grating spectroscopy." *Combustion and Flame* Vol. 199 (2019): pp. 249–257.

[7] Stopper, Ulrich, Meier, Wolfgang, Sadanandan, Rajesh, Stöhr, Michael, Aigner, Manfred and Bulat, Ghenadie. "Experimental study of industrial gas turbine flames including quantification of pressure influence on flow field, fuel/air premixing and flame shape." *Combustion and Flame* Vol. 160 No. 10 (2013): pp. 2103–2118.

[8] Wen, Xu, Hartl, Sandra, Dreizler, Andreas, Janicka, Johannes and Hasse, Christian. "Flame structure analysis of turbulent premixed/stratified flames with H2 addition considering differential diffusion and stretch effects." *Proceedings of the Combustion Institute* Vol. 38 No. 2 (2021): pp. 2993–3001.

[9] Hanson, Ronald K and Davidson, David F. "Recent advances in laser absorption and shock tube methods for studies of combustion chemistry." *Progress in Energy and Combustion Science* Vol. 44 (2014): pp. 103–114.

[10] Tang, Hao, Yang, Chaobo, Wang, Guoqing, Guiberti, Thibault F and Magnotti, Gaetano. "Raman spectroscopy for quantitative measurements of temperature and major species in high-pressure non-premixed NH3/H2/N2 counterflow flames." *Combustion and Flame* Vol. 237 (2022): p. 111840.

[11] Lewis, Ian R and Edwards, Howell. *Handbook of Raman spectroscopy: from the research laboratory to the process line*. CRC press (2001).

[12] Dibble, RW and Hollenbach, RE. "Laser Rayleigh thermometry in turbulent flames." *Symp.(Int.) Combust.,(Proc.);(United States)*. CONF-800809-. 1981. Sandia Lab, Livermore, CA.

[13] Daily, John W. "Laser induced fluorescence spectroscopy in flames." *Progress in energy and combustion science* Vol. 23 No. 2 (1997): pp. 133–199.

[14] Roy, Sukesh, Gord, James R and Patnaik, Anil K. "Recent advances in coherent anti-Stokes Raman scattering spectroscopy: Fundamental developments and applications in reacting flows." *Progress in Energy and Combustion Science* Vol. 36 No. 2 (2010): pp. 280–306.

[15] Cummings, EB. "Laser-induced thermal acoustics: simple accurate gas measurements." *Optics letters* Vol. 19 No. 17 (1994): pp. 1361–1363.

[16] Kiefer, Johannes and Ewart, Paul. "Laser diagnostics and minor species detection in combustion using resonant four-

Copyright © 2023 by ASME

wave mixing." *Progress in Energy and Combustion Science* Vol. 37 No. 5 (2011): pp. 525–564.

[17] Gutfleisch, M, Shin, DI, Dreier, T and Danehy, PM. "Mid-infrared laser-induced grating experiments of C2H4 and NH3 from 0.1–2 MPa and 300–800 K." *Applied Physics B* Vol. 71 No. 5 (2000): pp. 673–680.

[18] Stevens, R and Ewart, P. "Single-shot measurement of temperature and pressure using laser-induced thermal gratings with a long probe pulse." *Applied Physics B* Vol. 78 No. 1 (2004): pp. 111–117.

[19] Stampanoni-Panariello, A, Kozlov, DN, Radi, PP and Hemmerling, B. "Gas phase diagnostics by laser-induced gratings I. Theory." *Applied Physics B* Vol. 81 No. 1 (2005): pp. 101–111.

[20] Stampanoni-Panariello, A, Kozlov, DN, Radi, PP and Hemmerling, B. "Gas-phase diagnostics by laser-induced gratings II. Experiments." *Applied Physics B* Vol. 81 No. 1 (2005): pp. 113–129.

[21] Wu, Yulan, Zhuzou, Mingyang, Zhao, Tongxun, Ding, Pengji, Sun, Shaohua, Wang, Jijin, Liu, Zuoye and Hu, Bitao. "Gas-phase pressure measurement using femtosecond laser-induced grating scattering technique." *Optics Letters* Vol. 47 No. 7 (2022): pp. 1859–1862.

[22] Willman, Christopher, Le Page, Laurent M, Ewart, Paul and Williams, Benjamin AO. "Pressure measurement in gas flows using laser-induced grating lifetime." *Applied Optics* Vol. 60 No. 15 (2021): pp. C131–C141.

[23] Kozlov, DN. "Simultaneous characterization of flow velocity and temperature fields in a gas jet by use of electrostrictive laser-induced gratings." *Applied Physics B* Vol. 80 No. 3 (2005): pp. 377–387.

[24] Brown, Michael S and Roberts, William L. "Thermometry in pressurized sooting flames using laser-induced gratings." *Optical Technology in Fluid, Thermal, and Combustion Flow III*, Vol. 3172: pp. 492–503. 1997. SPIE.

[25] Sahlberg, Anna-Lena, Hot, Dina, Kiefer, Johannes, Aldén, Marcus and Li, Zhongshan. "Mid-infrared laser-induced thermal grating spectroscopy in flames." *Proceedings of the Combustion Institute* Vol. 36 No. 3 (2017): pp. 4515–4523.

[26] De Domenico, Francesca, Guiberti, Thibault F, Hochgreb, Simone, Roberts, William L and Magnotti, Gaetano. "Temperature and water measurements in flames using 1064 nm Laser-Induced Grating Spectroscopy (LIGS)." *Combustion and Flame* Vol. 205 (2019): pp. 336–344.

[27] Hayakawa, Akihiro, Yamagami, Tomohisa, Takeuchi, Kiyonori, Higuchi, Yasuhiro, Kudo, Taku, Lowe, Steven, Gao, Yi, Hochgreb, Simone and Kobayashi, Hideaki. "Quantitative measurement of temperature in oxygen enriched CH4/O2/N2 premixed flames using Laser Induced Thermal Grating Spectroscopy (LITGS) up to 1.0 MPa." *Proceedings of the Combustion Institute* Vol. 37 No. 2 (2019): pp. 1427–1434.

[28] Hot, Dina, Sahlberg, Anna-Lena, Aldén, Marcus and Li, Zhongshan. "Mid-infrared laser-induced thermal grating spectroscopy of hot water lines for flame thermometry." *Proceedings of the Combustion Institute* Vol. 38 No. 1 (2021): pp. 1885–1893.

[29] Brown, Michael S, Li, Yuanyuan, Roberts, William L and Gord, James R. "Analysis of transient-grating signals for reacting-flow applications." *Applied optics* Vol. 42 No. 3 (2003): pp. 566–578.

[30] Stampanoni-Panariello, A, Hemmerling, B and Hubschmid, W. "Temperature measurements in gases using laser-induced electrostrictive gratings." *Applied Physics B: Lasers & Optics* Vol. 67 No. 1.

[31] Shah, Priyav, Le Page, Laurent M and Williams, Benjamin AO. "Development and characterization of PILOT: a transportable instrument for laser-induced grating spectroscopy." *Optics Express* Vol. 31 No. 4 (2023): pp. 5872–5881.

[32] Goodwin, David G., Speth, Raymond L., Moffat, Harry K. and Weber, Bryan W. "Cantera: An object-oriented software toolkit for chemical kinetics, thermodynamics, and transport processes." (2023).

[33] Smith, Gregory P, Golden, David M, Frenklach, Michael, Moriarty, Nigel W, Eiteneer, Boris, Goldenberg, Mikhail, Bowman, C Thomas, Hanson, Ronald K, Song, Soonho, Gardiner Jr, William C et al. "Gri 3.0 mechanism, Gas Research Institute, 1999." *URL: http://www. me. berkeley. edu/gri_mech* .

[34] Runyon, Jon, Marsh, Richard, Bowen, Philip, Pugh, Daniel, Giles, Anthony and Morris, Steven. "Lean methane flame stability in a premixed generic swirl burner: Isothermal flow and atmospheric combustion characterization." *Experimental Thermal and Fluid Science* Vol. 92 (2018): pp. 125–140.

[35] Pugh, Daniel, Bowen, Philip, Crayford, Andrew, Marsh, Richard, Runyon, Jon, Morris, Steven and Giles, Anthony. "Catalytic influence of water vapor on lean blow-off and NOx reduction for pressurized swirling syngas flames." *Journal of Engineering for Gas Turbines and Power* Vol. 140 No. 6.

[36] Pugh, Daniel, Bowen, Philip, Valera-Medina, Agustin, Giles, Anthony, Runyon, Jon and Marsh, Richard. "Influence of steam addition and elevated ambient conditions on NOx reduction in a staged premixed swirling NH3/H2 flame." *Proceedings of the combustion institute* Vol. 37 No. 4 (2019): pp. 5401–5409.

[37] Pugh, DG, Bowen, PJ, Marsh, Richard, Crayford, AP, Runyon, Jon, Morris, Steven, Valera-Medina, A and Giles, Anthony. "Dissociative influence of H2O vapour/spray on lean blowoff and NOx reduction for heavily carbonaceous syngas swirling flames." *Combustion and flame* Vol. 177 (2017): pp. 37–48.

[38] Marsh, R, Runyon, J, Giles, A, Morris, S, Pugh, D, Valera-Medina, A and Bowen, P. "Premixed methane oxycombustion in nitrogen and carbon dioxide atmospheres: measurement of operating limits, flame location and emissions. Proceedings of the Combustion Institute." *Proceedings of the Combustion Institute* Vol. 36 No. 3 (2017): pp. 3949–3958.

,

 Copyright © 2023 by ASME